SINGLE PARTICLE MOTION STUDIES USING STEREO-VISION AND DIGITAL IMAGE PROCESSING

Carranza Chavez F.J.* and Zhang Y.
*Author for correspondence
Department of Mechanical Engineering,
University of Sheffield,
Mappin Building, Sheffield, S1 3JD
United Kingdom
E-mail: mep12fjc@sheffield.ac.uk

ABSTRACT

This paper proposes a new analysis technique to find the kinematics and dynamics of a single particle immersed in a fluid in a three-dimensional metric frame. Because the technique is entirely based on stereo-vision using only one camera attached to a stereo adapter, it offers great versatility and simplicity, and it does not cause any alteration to the physics of the studied phenomena, therefore ensuring that the interaction between the solid and its neighboring fluid stays undisturbed. Particle velocity, drag force, and orientation, represented through the angle of incidence, were estimated within the metric frame by means of digital image processing, vector algebra, and differential geometry operations. The methodology was first validated by analyzing the motion of three spheres settling in a fluid at different Reynolds numbers, where a close agreement between the coefficients of resistance determined here and those computed from literature correlations was obtained. The motion of two cylinders in free fall was then investigated, and it was found that at low Reynolds numbers a cylinder falls with fixed orientation in a straight path whilst for large Reynolds numbers it exhibits regular oscillation and travels in a sinusoidal fall path, thus causing an increment in the drag coefficient as the angle of incidence also augments.

INTRODUCTION

Traditionally the coefficient of drag C_D experienced by a particle moving in a fluid has been expressed as a function of the particle Reynolds number Re_P plus a shape descriptor for the cases when the solid is not spherical. However, it has also been suggested that the role played by the orientation of a non-spherical particle should be included since its position with respect to the main motion direction may change, depending on the value of Re_P, and this not only does modify the magnitude of the projected area but also alters the structure of the neighboring flow which in turn affects further the motion of the body [1-5]. According to Stringham et al. [2], in free fall conditions a disk does not settle with constant orientation once Re_P exceeds 400, but different patterns of fall appear. They reported regular oscillation of the disk up to $Re_P \sim 1000$, and combinations of oscillation, gliding, and tumbling for higher Re_P values.

NOMENCLATURE

a_T	[m/s^2]	Tangential acceleration
A_P	[m^2]	Particle projected area
$\boldsymbol{B}$	[-]	Binormal unit vector of the Frenet frame
C_D	[-]	Drag coefficient
d	[m]	Distance
D	[m]	Diameter
d_n	[m]	Nominal diameter
F_D	[N]	Drag force
g_T	[m/s^2]	Tangential component of the gravity acceleration
h	[-]	Digital stereo image
L	[m]	Length
m	[-]	Image point
m_P	[kg]	Particle mass
M	[m]	3D metric point
$\boldsymbol{N}$	[-]	Normal unit vector of the Frenet frame
P	[m]	Endpoint of the particle longest axis
Re_P	[-]	Particle Reynolds number
t	[s]	Time
$\boldsymbol{T}$	[-]	Tangential unit vector of the Frenet frame
u	[-]	Horizontal pixel coordinate
U_T	[m/s]	Terminal velocity
v	[-]	Vertical pixel coordinate
V_P	[m/s]	Particle velocity
X	[m]	Horizontal metric coordinate
Y	[m]	Vertical metric coordinate
Z	[m]	Depth metric coordinate

Special characters

α	[-]	Angle of attack
μ	[Pa·s]	Dynamic viscosity
ρ	[kg/m^3]	Density
σ	[-]	Aspect ratio
ϕ	[-]	Sphericity

Subscripts

C	Centroid
F	Fluid
P	Particle
W	World reference frame

In the case of a cylindrical particle, Marchildon et al. [1] found that it falls with fixed orientation, keeping its maximum projected area perpendicular to the main motion direction, as long as $Re_P < 80$. Above this value the cylinder may exhibit regular oscillation, nonetheless they confirmed that this one was always present once $Re_P > 300$. The presence of such oscillation was also proved by Yin et al. [4], and Chow and Adams [6].

In addition, as mentioned at the end of the first paragraph, it is vital that in any study of particle motion the interaction

between the solid and fluid remains uninterrupted. In fact, it has been estimated that even a settling sphere may achieve a value of C_D between 15 to 30% higher than that found for a fixed sphere exposed to a moving fluid as a consequence of the fluctuations and rotations that it may experience along its fall path [7].

For comparison purposes some of the correlations published in the literature to estimate the drag coefficient for spherical and non-spherical particles are listed in this paper. For the case of spheres, they are:

$$C_D = \frac{24}{Re_P}\left(1 + 0.15{Re_P}^{0.687}\right) + \frac{0.42}{1 + 4.25 \times 10^4 {Re_P}^{-1.16}} \quad (1)$$

$$C_D = 0.3 + \frac{23.5}{Re_P} + \frac{4.6}{\sqrt{Re_P}} \quad (2)$$

$$C_D = 2.689 + \frac{21.683}{Re_P} + \frac{0.131}{{Re_P}^2} - \frac{10.616}{{Re_P}^{0.1}} + \frac{12.216}{{Re_P}^{0.2}} \quad (3)$$

Equation (1) was proposed by Haider and Levenspiel [8] and is valid for $Re_P < 2.6\text{x}10^5$, Equation (2) was published by Yow et al. [9] and is valid for for $Re_P < 2\text{x}10^4$, and Equation (3), valid for $Re_P < 5\text{x}10^4$, was suggested by Terfous et al. [7]. For non-spherical particles, the correlation proposed by Haider and Levenspiel [8]

$$C_D = \frac{24}{Re_P}\left\{1 + \left[8.1716e^{-4.0655\emptyset}\right]{Re_P}^{0.0964 + 0.5565\emptyset}\right\} + \frac{73.69 Re_P\left(e^{-5.0748\emptyset}\right)}{Re_P + 5.378e^{6.2122\emptyset}} \quad (4)$$

was taken as a representative of the traditional way to estimate C_D. It is valid up to $Re_P < 2.5\text{x}10^4$. The parameter ϕ is known as the sphericity, which is defined as the ratio of the surface area of a sphere having the same volume as the particle under study to the actual particle surface area.

With the aim of improving the accuracy, other researchers have published correlations similar to Equation (4) but with the introduction of several geometrical parameters of complicated computation, nevertheless, in most of the cases the effects of angular variation were omitted. By using the angle of incidence α, defined as the angle between the particle major axis and the fluid velocity vector $\boldsymbol{V}$ (Figure 1), Zastawny et al. [5] have published an angle-dependent drag correlation of the form:

$$C_D = C_{D\alpha=0^\circ} + \left(C_{D\alpha=90^\circ} - C_{D\alpha=0^\circ}\right) sin^{2.12}\alpha \quad (5)$$

valid for $Re_P < 300$, and where

$$C_{D\alpha=0^\circ} = \frac{20.35}{{Re_P}^{0.98}} + \frac{2.77}{{Re_P}^{0.396}} \quad (6)$$

$$C_{D\alpha=90^\circ} = \frac{29.14}{{Re_P}^{0.97}} + \frac{3.66}{{Re_P}^{0.16}} \quad (7)$$

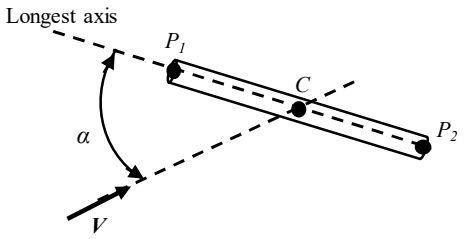

Figure 1 Angle of incidence of a non-spherical particle.

Although Equation (5) provides a clear dependence of the resistance on the orientation angle, in the numerical simulations the authors kept the particle static at each value of α, thus interrupting the solid/fluid interaction. For Equations (1) to (7), the drag coefficient and particle Reynolds number are calculated with the next relations:

$$C_D = F_D / 0.5 A_P \rho_f {V_P}^2 \quad (8)$$

$$Re_P = U_T d_n \rho_f / \mu \quad (9)$$

where F_D is the drag force, A_P the projected area normal to the direction on motion, ρ_f is the fluid density, V_P the particle velocity, U_T the particle terminal velocity, μ the fluid dynamic viscosity, and d_n the nominal diameter, defined as the diameter of a sphere of the same volume as the particle under concern.

As it can be seen from the revised literature the motion of a non-spherical particle in a fluid is accompanied by changes in its orientation and secondary motions, depending on the value of Re_P, which affect the value of the coefficient of resistance. The purpose of this paper is to experimentally find the effect of the orientation angle on the drag by means of high-speed stereo imaging and digital image processing, so that the solid/fluid interaction is unaltered. It does not aim to provide a new drag correlation but to improve the understanding of the phenomena.

SINGLE CAMERA STEREO VISION

The process of stereo vision consists on obtaining the three-dimensional (3D) information of a scene given at least a couple of two-dimensional (2D) images of it taken from slightly different points of view at the same instant. Therefore, as illustrated in Figure 2, the 3D coordinates of point M_W in the world reference frame $X_W Y_W Z_W$ can be determined given the coordinate pairs (u_1,v_1) and (u_2,v_2) of its two corresponding image points m_1 and m_2 on each image plane are known.

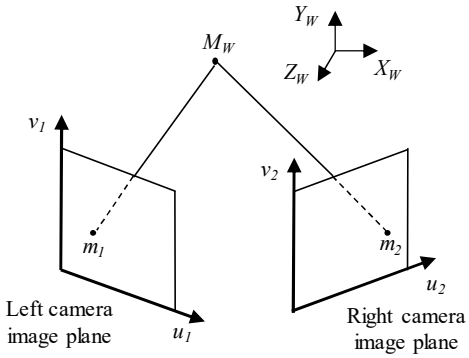

Figure 2 Conventional stereo system.

The procedure to find the 3D information of M_W involves the solution of the projective transformations between the real world and each camera 2D projective space plus the knowledge of the geometry between both cameras. These two requirements are met through the tasks of cameras calibration and the computation of the epipolar geometry of the stereo system. In this work the methodologies suggested by Zhang [10, 11] for camera calibration and epipolar geometry estimation, respectively, were followed. A series of computer programs were written in Matlab® for this purpose.

With the intention to avoid additional geometric differences due to misalignment issues and to maintain a simple visualization system, in this paper the process of stereo vision was accomplished using only one high-speed camera with a stereo adapter attached to its lens. The adapter chosen here is formed by an arrangement of four mirrors and it was manufactured by Pentax®. Its geometry and performance have been previously described by Wang et al. [12]. This stereo vision technique has been successfully used before to study the 3D structure of gas fuel flames [13].

EXPERIMENTAL STUDY

The particle motion studies performed in this paper involved two shapes: spherical and cylindrical. Because spheres do not possess an orientation angle and have a constant projected area, the analysis of their motion was done here as a method to test the reliability of the proposed stereo vision technique. On the other hand, since cylinders do exhibit changes in orientation, the analysis aimed to find whether those changes affect the value of the drag coefficient or not. The dimensions and properties of both particle shapes are summarized in Table 1.

Given the fact that a freely settling particle will always tend to the same terminal pattern of fall [1], there was no justification for a particular dropping method. Consequently, in this study the particles were dropped manually with the assistance of a funnel, as depicted in the schematic of the experimental installation portrayed in Figure 3. The employed working fluids were three mixtures of water and glycerin: 50%, 65%, and 80% by weight of glycerin, respectively. The experimental matrix is provided in Table 2.

Table 1 Dimensions and properties of the studied particles.

Shape	Material	ρ_P (kg/m^3)	D (mm)	L (mm)	d_n (mm)	Name
sphere	PTFE	2160	4.8	-	4.8	S1
sphere	PTFE	2160	6.4	-	6.4	S2
sphere	brass	8400	6.0	-	6.0	S3
cylinder	PTFE	2160	4.0	10.4	6.3	C1
cylinder	PTFE	2160	5.0	10.4	7.3	C2

At each case of the experimental matrix the particle was dropped three times, in average, and the stereo pictures were taken at 500 frames per second with a resolution of 1024x1024 pixels using a Photron® high-speed color camera and a Sigma® 24-70 mm macro lens coupled to the Pentax® stereo adapter.

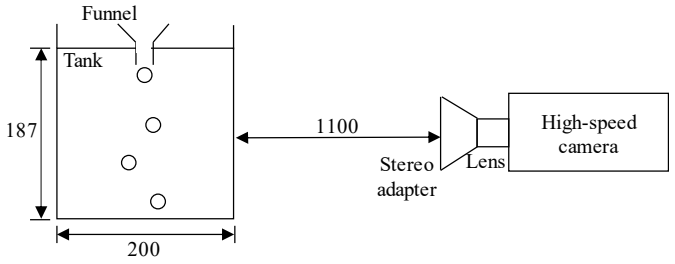

Figure 3 Simplified schematic of the experimental installation. Dimensions in mm, not to scale.

Table 2 Experimental matrix.

%wt. Glyc.	T_f (°C)	ρ_f (kg/m^3)	μ (Pa·s)	Particles
80	25.0	1205.5	0.047	S1, C1
65	30.0	1162.0	0.010	S2, S3
50	30.0	1121.1	0.004	C2

PROCESSING OF RESULTS

The particle points whose coordinates were reconstructed in 3D with the principle of stereo vision were the centroid C, and the longest axis extreme points P_1 and P_2, marked in Figure 1. However, in order to obtain such 3D information, the same points first needed to be detected on each recorded picture by means of digital image processing.

For every particle picture, the first step of image processing was the subtraction of the background picture (recorded before the particle entered the field of view), followed by a thresholding in order to completely isolate the pixel region representing the solid. The thresholding method proposed by Otsu [14] was applied here.

Once the only bright pixels are those corresponding to the particle, the coordinates X_C and Y_C of the centroid were computed by weighting the gray-scale intensity values of each image pixel as follows:

$$X_C = \frac{\sum u * h(u,v)}{\sum h(u,v)} \qquad Y_C = \frac{\sum v * h(u,v)}{\sum h(u,v)} \tag{10}$$

where h denotes the thresholded image. In Figure 4 the stereo image of a settling cylinder is shown before and after background removal and thresholding.

The final step of image processing was applied to the cylindrical particles only, and consisted on finding the perimeter pixels using the maximum intensity gradient principle recommended by Nishino et al. [15], so that P_1 and P_2 could be determined as the two perimeter points whose distance between each other was maximum. In Figure 5 the detected centroid and longest axis points for a cylinder are highlighted. All of the code required to perform the image processing operations listed in this paper was written in Matlab®.

(a) (b)

Figure 4 Stereo picture of a falling cylinder before (a) and after image enhancement (b).

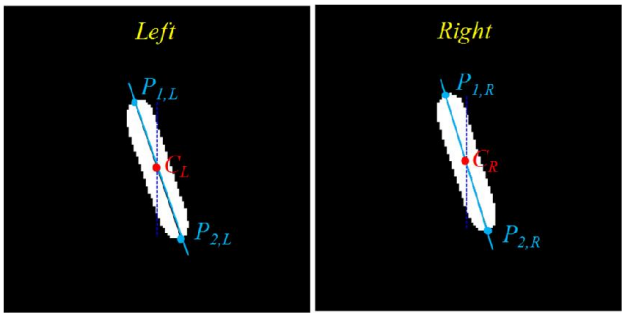

Figure 5 Centroid and longest axis points of a cylindrical particle.

Once the image processing steps were completed and the operations to obtain the 3D coordinates of each point finished, the velocity of any particle was found with the 3D coordinates of the centroid and the next equation:

$$V_P = d/\Delta t \tag{11}$$

where d represents the travelled distance at each time increment Δt. In addition, by following the approach suggested by Veldhuis et al. [16], the instantaneous drag force experienced by the solid was also estimated. They said that if a Frenet reference frame (formed by three unit vectors: tangent $\boldsymbol{T}$, normal $\boldsymbol{N}$, and binormal $\boldsymbol{B}$) is attached to the 3D curve of the centroid, the magnitude of the drag can be approximated from a force balance in the tangent direction as follows:

$$F_D = \left(1 + \frac{\rho_f}{2\rho_P}\right) m a_T - \left(1 - \frac{\rho_f}{\rho_P}\right) m g_T \tag{12}$$

where m is the mass of the solid, a_T is the tangential acceleration, and g_T is the component of the acceleration due to gravity also in the tangential direction. Finally, being $\boldsymbol{P_1P_2}$ the 3D vector representing the particle longest axis and $\boldsymbol{V_P}$ the 3D velocity vector in the tangential direction $\boldsymbol{T}$, it was possible to find the angle of incidence as the angle between those two vectors with the following equation:

$$\alpha = arccos\left(\frac{\boldsymbol{P_1P_2} \cdot \boldsymbol{V_P}}{|\boldsymbol{P_1P_2}||\boldsymbol{V_P}|}\right) \tag{13}$$

ANALYSIS OF RESULTS

Spheres

The settling trajectories described by the stereo 3D reconstructed coordinates of the centroids of spheres S1, S2, and S3 are plotted in Figure 6, where it can be observed that despite being considerable smooth, the paths deviated from a straight line as Re_P increased from (a) to (c). This can be attributed to changes in the structure of the flow around each solid as the inertial force augments. The calculation of Re_P is explained in the coming paragraphs.

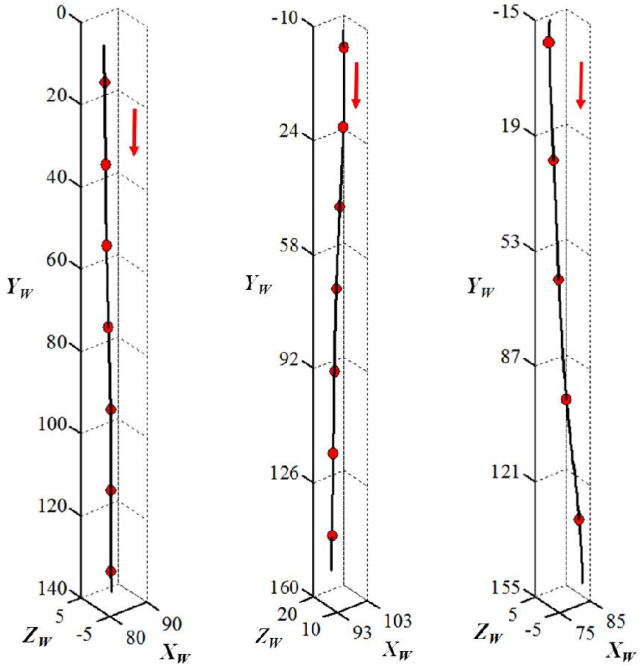

(a) (b) (c)

Figure 6 Fall paths of the spheres S1 (a), S2 (b), and S3 (c).

Choosing sphere S2 as example of analysis, its instantaneous velocity was computed with Equation (11) and plotted against time in Figure 7. The drag force it experienced during the fall was estimated with Equation (12) and also included in Figure 7.

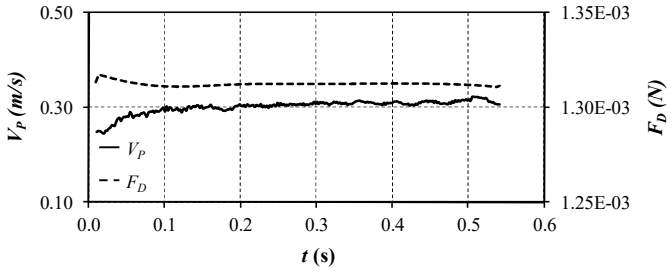

Figure 7 Velocity and drag force plots of sphere S2.

In Figure 7 it can be appreciated how the velocity of the particle increased until it reached terminal conditions at, approximately, 0.2 s after entering the field of view. This moment corresponded to $U_T \sim 0.32$ m/s and, from Equation (9), to $Re_P = 238$. Also from Figure 7, it can be noticed that within terminal velocity conditions the drag remained practically

constant at 1.31 mN, which substituted in Equation (8) resulted in $C_D = 0.70$.

By doing a similar procedure for the other two spheres, S1 and S3, it was obtained: $U_T \sim 0.12$ m/s, $Re_P = 15$, $C_D = 3.37$, and $U_T \sim 0.93$ m/s, $Re_P = 648$, $C_D = 0.56$, respectively. In Figure 8 a comparison between these drag values and those calculated from Equations (1) to (3) is shown graphically, where a close agreement can be appreciated.

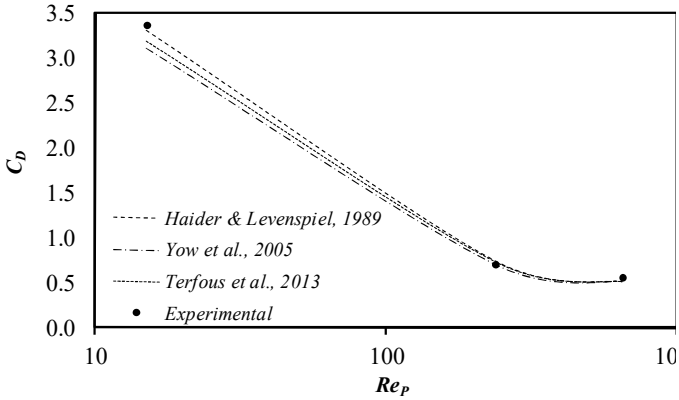

Figure 8 Drag coefficients comparison.

In Figure 8, the difference between the experimental results and those from the mentioned literature correlations was not larger than 10%, therefore it can be said that the proposed methodology to estimate the dynamics of a particle out of its 3D trajectory only is valid.

Cylinders

From the images of the settling cylinders C1 and C2 recorded by the right camera in Figures 9a and 9b, it can be noticed that the first cylinder displayed a relatively straight path with fixed orientation whilst the second one described a sinusoidal trajectory accompanied by some regular oscillation. These behaviors agree with the results published by Marchildon et al. [1], Yin et al. [4], and Chow and Adams [6].

By taking advantage of the 3D visualization technique, the trajectories of the centroids and orientations of the longest axis, for both cylinders, can also be plotted within the world reference frame as shown in Figures 10a and 10b where at some randomly chosen positions the centroids were colored in red, the endpoints P_1 and P_2 in green, and the longest axis lines in blue.

The terminal velocity values and particle Reynolds numbers of both cylinders were also obtained from the same procedure applied to the spheres. Hence, the results were: $U_T \sim 0.14$ m/s, $Re_P = 23$ for C1, and $U_T \sim 0.32$ m/s, $Re_P = 655$ for C2, respectively.

In Figure 11, the drag forces experimented by each cylinder are plotted against time, where a continuous increment, even within the final conditions interval, was registered for particle C2 whilst C1 kept a constant value of 1.23 mN after conditions of terminal velocity were reached.

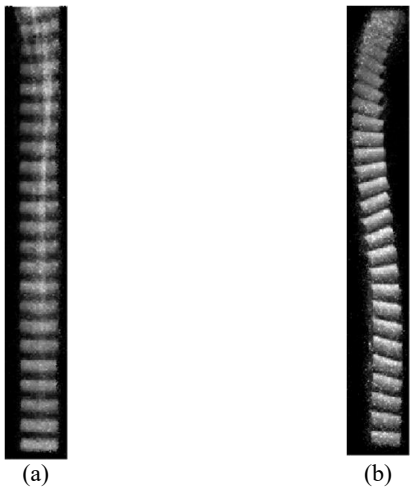

Figure 9 Images of the settling cylinders C1 and C2, respectively, registered by the right virtual camera.

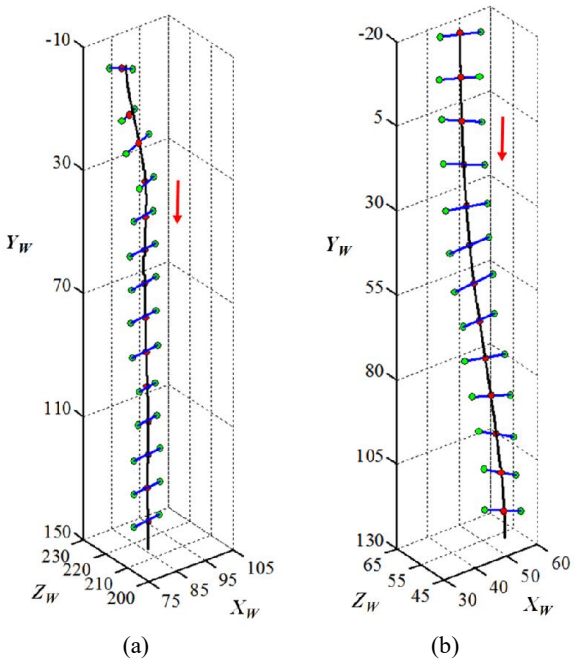

Figure 10 3D plots of cylinders C1 and C2 centroid trajectories. The blue lines denote the longest axis.

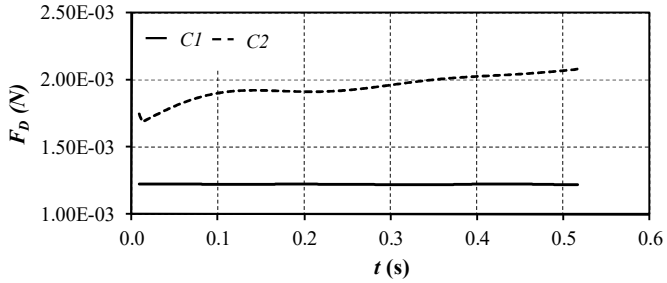

Figure 11 Drag force plots of cylinders C1 and C2.

For each time increment the angle of incidence of cylinder C2 was computed with Equation (13), and the results were also

plotted against time as illustrated in Figure 12, where a regular oscillation pattern between 65 and 90 degrees, approximately, can be appreciated.

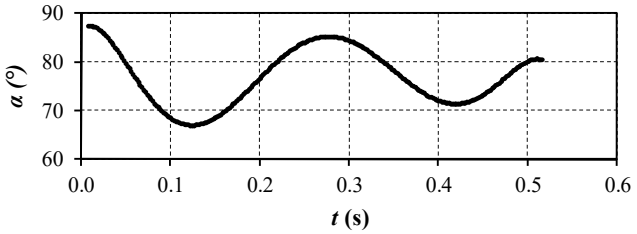

Figure 11 Variation of the angle of incidence with time for cylinder C2.

By estimating the projected area as $A_P = LDcos\alpha$ and using Equation (8) to determine C_D, a plot of drag vs orientation can be generated, as done in Figure 13 where only the terminal conditions interval is graphed. From this plot, it can be noticed that the coefficient of resistance increases from 0.70 to 0.75 as α augments, similarly to the results reported by Zastawny et al. [5] at $Re_P = 300$ for the same angle interval.

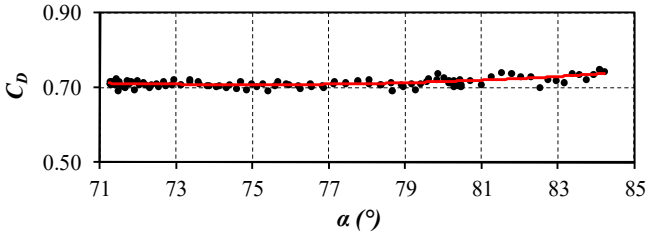

Figure 12 Coefficient of resistance variation with the angle of incidence for cylinder C2.

Because cylinder C1 kept a fixed orientation the projected area was calculated as $A_P = LD$, and given that $F_D \sim 1.23$ mN, the obtained value for C_D was 2.5. The value found with Equation (4) was 2.8, which is in good agreement. However, for cylinder C2, Equation (4) gave 0.9, which is an evident overestimation of the drag.

CONCLUSIONS

The settling motion of spherical and cylindrical particles was studied using 3D stereo vision and digital image processing, estimating the kinematics and dynamics only out of the 3D centroid trajectory coordinates, and the longest axis endpoints for the case of cylinders.

For the spherical particles, a close agreement between the C_D values found here and those determined from three published correlations was obtained, suggesting that the methodology of analysis proposed in this paper not only is original, but also valid.

For the cylinders, it was found that at low Re_P and terminal velocity conditions the particle settles with fixed orientation and displays a relatively straight trajectory. The drag coefficient also remains remarkably constant. However, at high Re_P, regular oscillation characterizes the orientation of the cylinder and its centroid displacement describes more a sinusoidal path. In addition, the value of C_D exhibits a light increment as the angle of incidence also augments.

REFERENCES

[1] E. K. Marchildon, A. Clamen, and W. H. Gauvin, "Drag and oscillatory motion of freely falling cylindrical particles," *The Canadian Journal of Chemical Engineering,* vol. 42, pp. 178-182, 1964.

[2] G. E. Stringham, D. B. Simons, and H. P. Guy, "The behaviour of large particles falling in quiescent liquids," U. D. o. t. Interior, Ed., ed. Washington D.C.: Geological Survey Professional Paper 562-C, 1969, pp. 4-43.

[3] D. Besnard and F. H. Harlow, "Nonspherical particles in two-phase flow," *International Journal of Multiphase Flow,* vol. 12, pp. 891-912, 1986.

[4] C. Yin, L. Rosendahl, S. Knudsen Kær, and H. Sørensen, "Modelling the motion of cylindrical particles in a nonuniform flow," *Chemical Engineering Science,* vol. 58, pp. 3489-3498, 2003.

[5] M. Zastawny, G. Mallouppas, F. Zhao, and B. van Wachem, "Derivation of drag and lift force and torque coefficients for non-spherical particles in flows," *International Journal of Multiphase Flow,* vol. 39, pp. 227-239, 2012.

[6] A. Chow and E. Adams, "Prediction of Drag Coefficient and Secondary Motion of Free-Falling Rigid Cylindrical Particles with and without Curvature at Moderate Reynolds Number," *Journal of Hydraulic Engineering,* vol. 137, pp. 1406-1414, 2011.

[7] A. Terfous, A. Hazzab, and A. Ghenaim, "Predicting the drag coefficient and settling velocity of spherical particles," *Powder Technology,* vol. 239, pp. 12-20, 2013.

[8] A. Haider and O. Levenspiel, "Drag coefficient and terminal velocity of spherical and nonspherical particles," *Powder Technology,* vol. 58, pp. 63-70, 1989.

[9] H. N. Yow, M. J. Pitt, and A. D. Salman, "Drag correlations for particles of regular shape," *Advanced Powder Technology,* vol. 16, pp. 363-372, 2005.

[10] Z. Zhengyou, "A flexible new technique for camera calibration," *Pattern Analysis and Machine Intelligence, IEEE Transactions on,* vol. 22, pp. 1330-1334, 2000.

[11] Z. Zhang, "A new multistage approach to motion and structure estimation: from essential parameters to euclidean motion via fundamental matrix," INRIA Sophia-Antipolis, Cedex, 1996.

[12] R. Wang, X. Li, and Y. Zhang, "Analysis and optimization of the stereo-system with a four-mirror adapter," *Journal of the European Optical Society - Rapid publications; Vol 3,* 2008.

[13] Q. Wang, J. Yang, H. W. Huang, Y. Zhang, and C. Zhao, "Three-dimensional investigation of the dynamics of a propane diffusion flame," *Fuel,* vol. 116, pp. 448-454, 2014.

[14] N. Otsu, "A threshold selection method from gray-level histograms " *IEEE Transactions on Systems, Man, and Cybernetics* vol. SMC-9, pp. 62-66, 1979.

[15] T. Koichi Nishino and Hiroyuki Kato and Kahoru, "Stereo imaging for simultaneous measurement of size and velocity of particles in dispersed two-phase flow," *Measurement Science and Technology,* vol. 11, p. 633, 2000.

[16] C. H. J. Veldhuis, A. Biesheuvel, and D. Lohse, "Freely rising light solid spheres," *International Journal of Multiphase Flow,* vol. 35, pp. 312-322, 2009.